UC Irvine

Title

Microcalcification Detection with Low Dose Dedicated Breast CT Based on CdTe Photon-counting Detector

Permalink

https://escholarship.org/uc/item/7546v2dg

Author

Ho, Fong Chi

Publication Date

2022

Copyright Information

Peer reviewed|Thesis/dissertation

UNIVERSITY OF CALIFORNIA,
IRVINE

Microcalcification Detection with Low Dose Dedicated

Breast CT Based on CdTe Photon-counting Detector

THESIS

submitted in partial satisfaction of the requirements
for the degree of

MASTER OF SCIENCE

in Electrical and Computer Engineering

by

Fong Chi Ho

Thesis Committee:
Professor Sabee Molloi, Chair
Chancellor's Professor Hamid Jafarkhani
Professor G. P. Li

2022

TABLE OF CONTENTS

Page

LIST OF FIGURES

Page

LIST OF TABLES

ACKNOWLEDGEMENTS

ABSTRACT OF THE THESIS

Microcalcification Detection with Low Dose Dedicated

Breast CT Based on CdTe Photon-counting Detector

by

Fong Chi Ho

Master of Science in Electrical and Computer Engineering

University of California, Irvine, 2022

Professor Sabee Molloi, Chair

This study investigated the detectability of microcalcifications (MCs) using a low dose dedicated computed tomography (CT) system with a Cadmium Telluride (CdTe) photon-counting detector of 75 µm pixel pitch in a 12 cm diameter postmortem breast and an accredited mammography phantom. Calcium carbonate grains with size of 125–250 µm were inserted into the postmortem breast. Phantoms were imaged at 65 kVp with a mean glandular dose (MGD) of 1.7–21 mGy and reconstructed by Filtered back-projection (FBP) algorithm and analytical iterative reconstruction (AIR) at a voxel size of 50 μm^3. Three and two blinded readers rated the visibility of MCs and the three groups of targets based on a 4-point scale and ACR phantom scoring scheme for the postmortem breast and ACR phantom, respectively. The MCs and targets detectability were evaluated by the averaged area under the receiver operating characteristic curves and the average score across readers, accordingly. The ACR phantom study showed an average score of 5.5 and 4.75 for fibers, 3.5 and 2.5 for speck groups, and 4.5 and 3.5 for masses at 3 mGy for AIR and FBP reconstruction, respectively. The postmortem breast study showed detectability of MCs larger than 125 µm with AUC greater than 0.912±0.038 at a MGD of 3 mGy and maintained an AUC greater than 0.843±0.038 at a mean glandular dose of 2 mGy.

1. INTRODUCTION

Breast cancer is the most common cancer diagnosed and is the second leading cause of cancer-related death among women.[1] Its incidence rate has been increasing by 0.5% per year since the mid-2000s, resulting in part to the continuous fertility rate declination.[2] Microcalcifications (MCs) are present in over 30% of all malignant breast lesions and 50% of the malignant infraclinical breast lesions.[3] Furthermore, MCs are the only imaging feature of invasive breast cancer in 32% of the cases.[3] Therefore, achieving high detectability of MCs is crucial for early-stage breast cancer diagnosis.

Full field digital mammography (FFDM) is the gold standard to detect MCs in breast cancer screening. However, the superimposition of breast mammographic images compresses a three-dimensional image into two-dimensional projections, resulting in the difficult MCs detection from the overlapped structures of the anatomical breast and low contrast between glandular and pathologic tissue.[4] Some radiologists have suggested and preferred to use FFDM coupled with digital breast tomosynthesis (DBT) because some cancers have a higher detection rate on one of the two views, given the limited 3D resolution of DBT.[5] However, the radiation received by the patient is almost doubled. Compared to the need of multiple acquisitions at different views to confirm a lesion in FFDM, CT provides a truly isotropic 3D images to detect lesions on any desired plane from a single acquisition. Moreover, cone-beam breast CT provides higher image quality of breast tissue than with mammography in the lateral, medial, and posterior views.[6]

Traditional CT with flat panel detector shows worse detection of MCs than digital mammography (DM) systems and produces images with poor spatial resolution.[7] Instead,

1

photon-counting breast CT (pcBCT) capable of detecting MCs of 100 μm at a dose below 5 mGy with a higher spatial resolution. Other Phantom studies also shows an improvement of MCs detection by reducing the pixel dimensions with a high-resolution detector.[8]

For current CT reconstruction, Feldkamp-type filtered back projection (FBP) method is widely used because it is computationally fast and easily implemented based on a single reconstruction to generate images with low signal-to-noise ratio (SNR).[9] Numerous advancements in reconstruction have been proposed to improve the SNR, such as the iterative algorithms (IR) that use multiple repetitions of correction and estimation to produce higher image quality than FBP, and have high potential for reducing the radiation dose.

In the present study, we have developed a prototype CT system to capture the projections of ACR mammography phantom and postmortem breast with a Cadmium Telluride (CdTe) based photon-counting detector and reconstruct them using both FBP and IR algorithms. The visibility of the MCs and details in multiple sizes and doses were investigated.

2. MATERIALS AND METHODS

2.1. Phantoms

A mammographic accreditation phantom (VICTOREEN, INC. Mammographic Accreditation phantom, H-575) and a postmortem breast were used in this study. The phantom was in dimension of 10.15 (w) x 10.8 (l) x 4.4 cm (h). It consisted of three types of target object, nylon fibers in thicknesses of 1.56, 1.12, 0.89, 0.75, 0.54 and 0.4 mm; Al2O3 specks groups of 6 in sizes of 0.54, 0.40, 0.32, 0.24, and 0.16 mm; tumor-like masses in diameters of 20, 10, 7.5, 5 and

2

2.5 mm. The ACR phantom was placed in a 12 cm diameter cylindrical cup with 0.15 cm wall

thickness filled with water to maintain a cylindrical shape for cone-beam CT reconstruction.

A 12 cm postmortem breast was acquired through the Willed Body program in the School of

Medicine at the University of California, Irvine. The breast weighted 610 grams and placed in a

cylindrical polystyrene tube with 13.5 cm inner diameter and 1.5 cm wall thickness. An opening

of 2 (w) x 1.5 (l) x 0.5 cm (h) was cut on the side of the breast to place inserts with multiple sizes

of calcium grains. Calcium carbonate grains (Thermo Fisher Scientific, New Jersey) in size of

125–140, 160–185, and 215-250 µm were filtered by multiple sizes of mesh and distributed in

the inserts to mimic MCs. Figure 1a presented the reconstructed CT image of the postmortem

breast at 12 mGy with the insert. Figure 1b shows a magnified image of the insert where the

white specks group indicated the existence of 215 - 250 µm calcium carbonate.

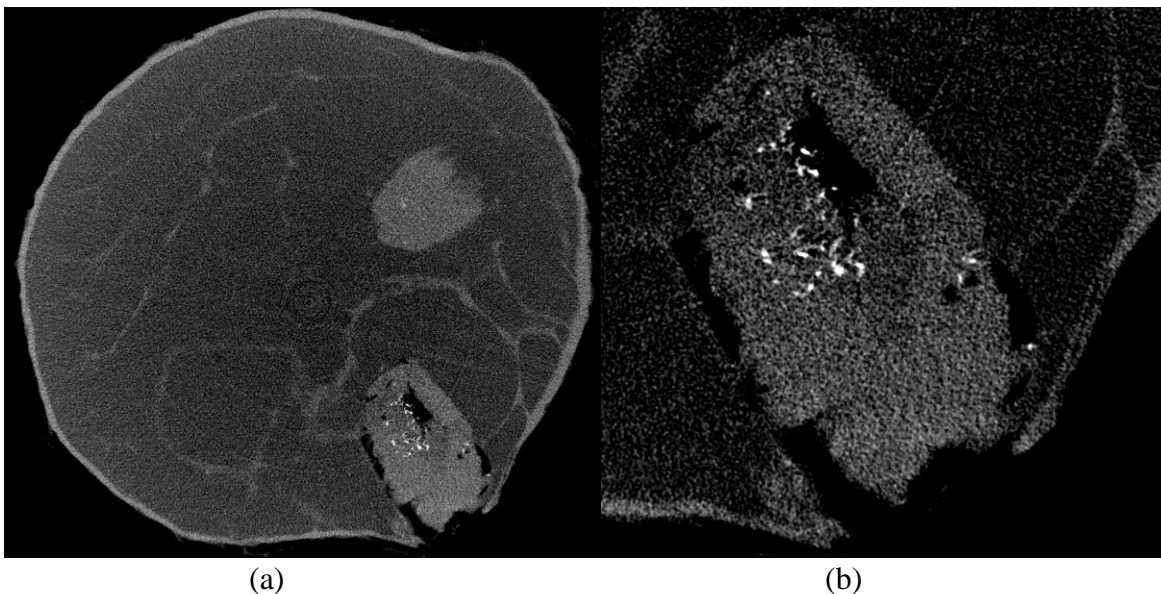(a)   (b)

Fig. 1(a). The reconstructed CT image of the postmortem breast at 12 mGy with
microcalcification inserts. (b). The extracts of (a) with 250 µm calcification.

2.2. Imaging Techniques

2.2.1. CdTe CT system

The photon-counting breast CT system consisted of a tungsten x-ray tube (Toshiba America Inc., SAPPHIRE-150TH, Irvine, CA) coupled with a Phillips OptimusM200 x-ray generator, and a CdTe-based photon-counting detector (DECTRIS Ltd, SANTIS 1604 HR, Switzerland) mounted on an optical bench. A high precision motor (Kollmorgen Goldline DDR D062M, Danaher Motion, Wood Dale, IL) serving as the rotational stage was mounted on a translation stage controlled by twostep motors, rendering both vertical and horizontal translations.
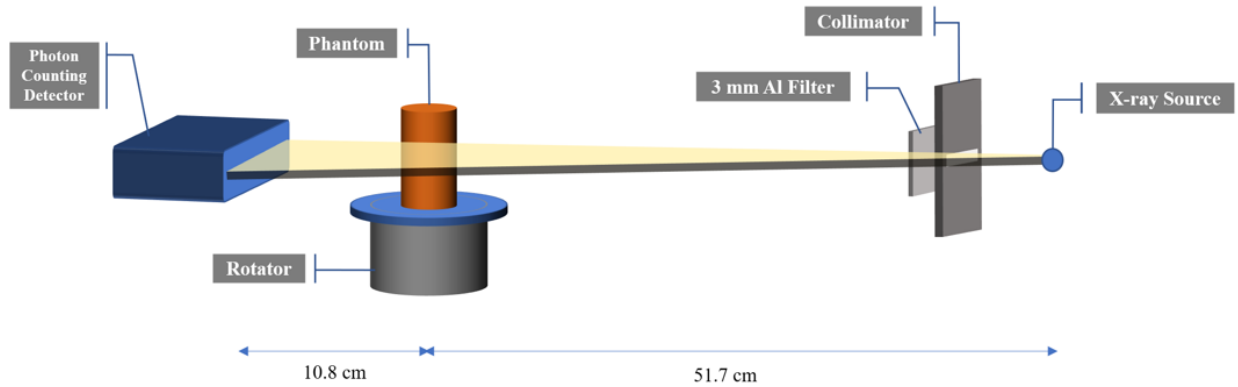

Fig. 2. Schematic drawing of the CT system geometry.

The photon-counting detector had a pixel size of 0.75 mm x 0.75 mm and converted x-ray photons directly into electric charge. The matrix of the detector is 2070 x 514 pixels with 5944.41 mm^2 active area. A simple sketch of the CdTe CT system is presented in Fig.2. The CdTe detector communicated with the workstation via a PowerEdge R230 detector control unit (Dell Inc., Round Rock, Texas, USA) through a dedicated GUI interface. The source-to-detector distance (SID) and the source-to-object distance (SOD) were 62.5 cm and 51.7 cm, respectively, leading to a magnification of 1.2.

CT scans were acquired at 65 kVp with a tube current of 2 mA with a 0.4 mm focal spot size. A threshold of 20keV was introduced to limit the electronic and quantum noise in the projections by removing low energy photon signals. A full CT scan at 0.5 rpm covering 360 degree of object rotation yielded a total of 1480 frames. The beam was prefiltered by collimator and 3 mm aluminum. The mean glandular dose (MGD) for a 12 cm breast is approximately 12 mGy at this setting. Virtual dose reduction was performed by reducing number of projections for reconstruction to obtain lower dose images.

2.2.2. Correction of projection images

All projections acquired with the CdTe detector were flat field corrected for detector nonuniformity using an averaged projection from 300 open field projections. The gain Gi was calculated by

$$G_i = \frac{\sum_{k=1}^{N} P_k}{P_i N}$$

Where P_i was the ith pixel value of the averaged flat-field image projection and N was the total pixel number. The corrected pixel values P_{ci} for subsequent scans of projections were calculated by

$$P_{ci} = G_i P_{ri}$$

Where P_{ri} was the ith pixel value of the uncorrected projection.

The horizontal and vertical intermodular gaps on the projections were corrected to maintain consistent mean and standard deviation values by filling the mean pixel value of pixels adjacent to the gaps and adding gaussian noise from the adjacent 12 pixels. Dead and hot pixels were corrected by a 5 x 5 median mask filter. Figure 3a and 3b shows the corrected projections of

ACR phantom and the postmortem breast, respectively. The ACR phantom was placed in the cylindrical cup filled with water.

Herman's beam-hardening correction method was used.[11] The polynomial calculation showed as

$$S_{out} = a_0 + a_1 S_{in} + a_2 S_{in}^2 + a_3 S_{in}^3$$

Where the S_{in} and S_{out} were the input and output of the log signal attenuation value calibrated against air, which was defined by

$$S = \ln\left(\frac{I_0}{I}\right) = \mu d$$

I and I_0 were the intensity values with and without target, μ the attenuation coefficient and d the path length through the target. Coefficient a_0 was 0 in practical case. a_1, a_2 and a_3 were obtained by the linear fitting of attenuations across 3 different thicknesses of water with slope μ.
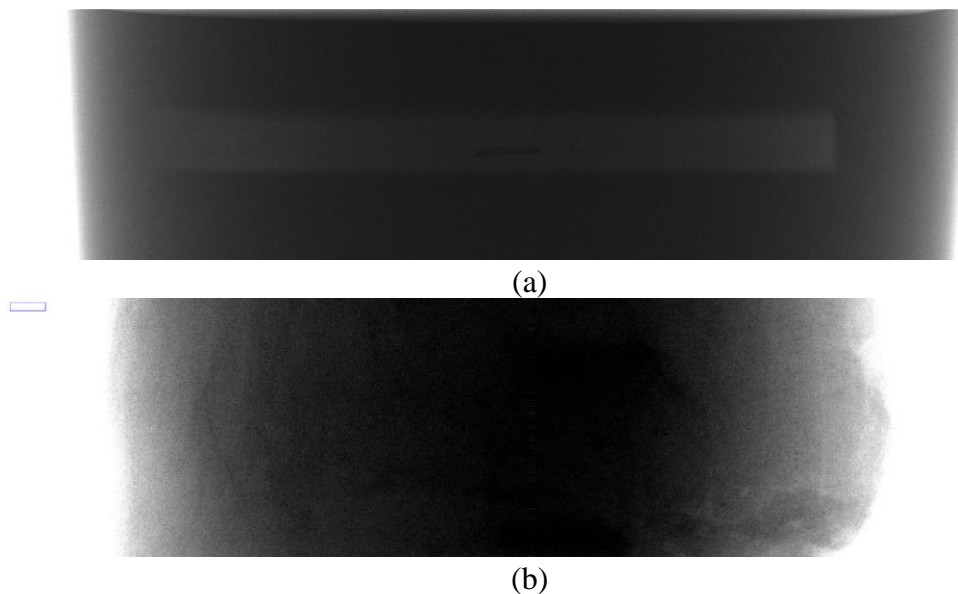

(a)

(b)

Fig 3. Fully corrected projection of the (a) ACR mammography phantom and (b) postmortem breast

2.3. Reconstruction

Images from both filtered back-projection (FBP) and analytical iterative reconstruction (AIR) were reconstructed with a sharp kernel of 50 x 50 x 100 μm^3 voxel size for high-resolution MCs analysis. Apart from the FBP method using hamming filter and Parker Weight filter, AIR method was used based on the modified proximal forward-backward splitting (PFBS) algorithm[12,13]. FDK was used for the analytical reconstruction method in updating the filtered data fidelity term, and a total-variation sparsity regularization was used to update the regularization term.[14] AIR decoupled data fidelity and image regularization in two iterative steps. In the first step, the image formed a projection residual by projecting it to the projection domain, then the residual was reconstructed by FDK into a residual image which was weighted together with previous image iterated to form the next image iteration, by

$$x^{n+\frac{1}{2}} = x^n - sF(Ax^n - y)$$

Where x was the reconstructed image, y was the projections, s the algorithm parameters, A the projection operator discretized from the x-ray transform, and F the FDK operator indicated as
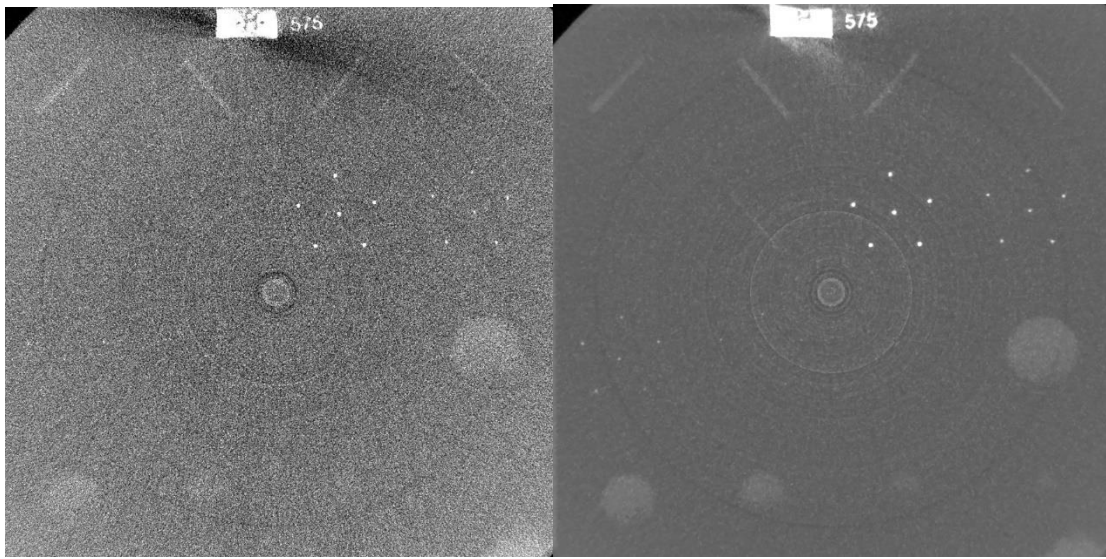
$$F(y) = B \cdot C \cdot Wy$$

Where B was the back-projection operator, C the filtering operator, and W the weights operator. In the second step, the image denoising was done by

$$x^{n+1} = \arg\min_x \frac{1}{2}\left\|x - x^{n+\frac{1}{2}}\right\|_2^2 + s\lambda\|\nabla x\|_1$$

Where λ was the regularization parameter.

Figure 4a and 4b shows the same reconstructed image at 21 mGy of ACR phantom using FBP and AIR algorithms, respectively.

Fig. 4. Reconstructed image of ACR mammography phantom using (a) FBP algorithm and (b) iterative reconstruction algorithm.

2.4. Reader Study

The evaluation of the ACR phantom was performed by a radiologist and a diagnostic medical physicist with over 8 and 10 years of experience in mammography, respectively. The readers reviewed 10 stacks of CT reconstructed ACR phantom images at 10 doses ranging from 1.5 mGy to 21 mGy. Each stack consisted of 12 consecutive slices with adjustable window size, magnification, and levels for the optimal visibility. Each fiber, group of specks, and mass was rated with score 0, 0.5 or 1, according to the ACR Digital Mammography Phantom Scoring Key.[15]

The evaluation of microcalcifications in postmortem breast images was performed by 3 blinded readers, with breast CT imaging experiences ranging from 1 to 8 years. In the first stage, 3 readers performed a MC size measurement study. Each measured the full width at half maximum (FWHM) on a line plot across a single MC for 20 MCs in random at all doses.

In the second stage, the MCs classification study was performed. Each reader underwent a training set, which contained 9 images with MCs in range of 125-140 μm, 160-185 μm and 215-250 μm at 1.7mGy, 6 mGy and 12 mGy independently, and 3 images without MCs. Readers were to learn the existence of specks and familiarize themselves with the evaluation tasks. They were allowed to adjust the window settings, magnification, and levels. 240 MCs images (8 doses x 3 sizes x 10 images) combined with 56 control images without MCs (8 doses x 7 images) were grouped into 296 images in random order for the study. Without the disclosure of ground truth, the readers identified the existence of specks using a 4-point scale (1 = certainly absent, 2 = possibly absent, 3 = possibly present, 4 = certainly present).

2.5. Data Analysis

For the ACR phantom, an average of the total score per test object across all readers was calculated and compared to the full score of 6, 5, and 5 for fibers, specks, and masses, respectively. For the postmortem breast, paired design of receiver operating characteristic (ROC) curves for each size of MCs was analyzed using NCSS statistical software version 2022 (NCSS, LLC. Kaysville, Utah, USA). The area under the empirical ROC curve (AUC) was calculated using summation of trapezoid areas under the connected points making up the ROC curve.[16] The accuracy in MCs detection was evaluated by the averaged AUC across the readers for each MC size and dose. The differences in AUC, standard error and confidence level between different sizes of MC of the same dose level were evaluated by z-test and p-value hypothesis test to indicate statistical significance.

3. RESULTS

Figure 5a and 5b showed the magnified areas of ACR phantom with five different sizes of Al_2O_3 specks at different doses, reconstructed by FBP and AIR algorithms, respectively. 320, 400, and 540 μm specks were visible at all doses in AIR images, while only 540 μm specks were visible at all doses in FBP images. 320 and 400 μm specks were visible for doses larger than 3 and 3.5 mGy, respectively. 160 μm and 240 μm specks for both FBP and AIR images were difficult to differentiate from the background noise, yet visible by adjusting the image setting. The same group of specks was visible on consecutive slices because of difficulty in positioning the phantom horizontally in the water for the cone beam scanning.

Fig.5 Magnified areas with five varied sizes of specks are shown in the images of ACR phantom reconstructed by (a) FBP and (b) IR algorithms. Each column shows the same size of cluster with different MGDs. All images in a column have the same window and level.

The individual rating from each reader and the average rating for specks, fibers and masses using FBP and AIR were recorded in figures 6a and 6b. An average score of 5.5 and 4.75 for fibers, 3.5 and 2.5 for speck groups, and 4.5 and 3.5 for masses at 3 mGy were calculated for AIR and FBP reconstruction, respectively.
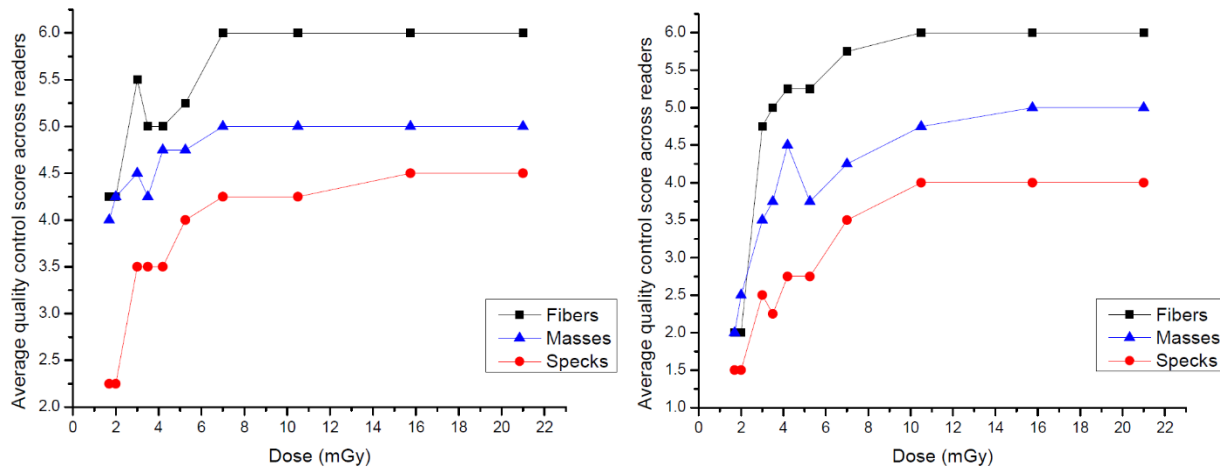
Figure 6. The average quality control score of the ACR phantom images across readers, reconstructed by (a) IR and (b) FBP methods.

Figure 7 shows the line plot measurements of a single MC with the size in range of 125-140 µm in postmortem breast using ImageJ (U. S. National Institutes of Health, Bethesda, MD) for data collection. The mean and standard error of single MC diameter across 3 readers are shown in table I. The averaged MC diameter of 125-140 µm, 160-185 µm and 215-250 µm were calculated as 148 µm, 195.3 µm, and 269.2 µm, respectively. The mean measurement of each size of MCs were comparable to the actual range of MCs, indicating no clustering of the MCs to form calcification of larger size.
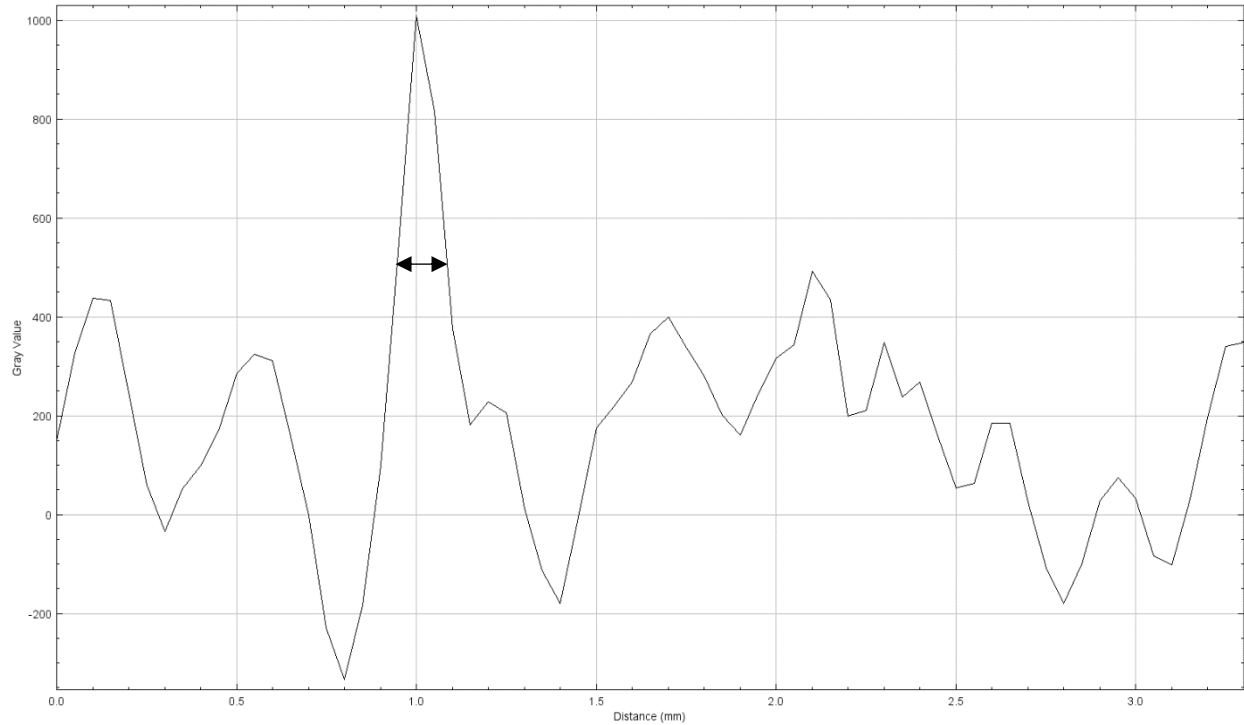
Fig. 7. Line plot measurement across a single calcification of size 140 μm at 12 mGy. The diameter of the calcification was measured at full width at half maximum (FWHM).

Table I. The mean and standard error measurement of sizes of microcalcification in the postmortem breast at 12 mGy. Twenty specks per observer per size were measured.

Microcalcification measurement	125 - 140 um		160 - 185 um		215 - 250 um	
	Mean	Std. Error.	Mean	Std. Error.	Mean	Std. Error.
Observer 1	147.5	7.7	193.5	7.8	282.5	8.3
Obsever 2	142.5	7.5	190	8.6	267.5	11.0
Observer 3	154	9.3	202.5	9.2	257.5	11.0
Average	148	8.2	195.3	8.5	269.2	10.1

Figure 8 shows the magnified areas with 3 different sizes of MCs at different doses in postmortem breast, reconstructed by FBP method. Each column shows the same size of cluster with different MGDs. All images in a column have the same window, level and contrast. In FBP images, 160-185um and 215-250 μm MCs were clearly visible with well-preserved shape at 3 mGy, and with deformed shape in 2.4, 2 and 1.7 mGy. MCs of 125-140 μm were visible at 2.4

12

mGy with deformed shape, and difficult to differentiate from background noise at 1.7 and 2 mGy
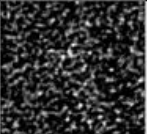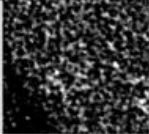
without adjusting the image setting.
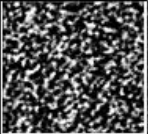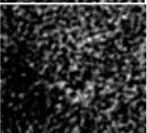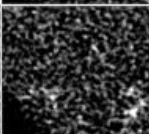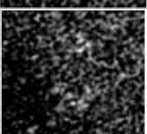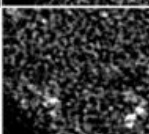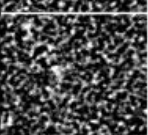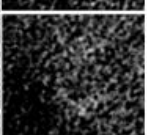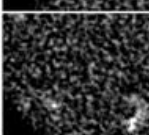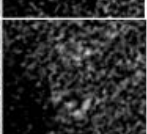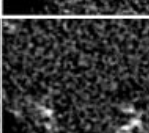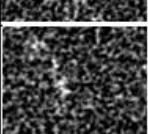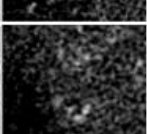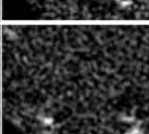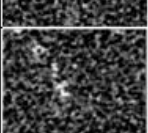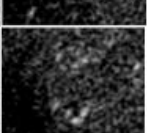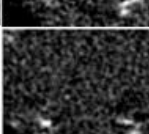
Fig. 8 Magnified areas with three varied sizes of microcalcifications are shown in the images of postmortem breast reconstructed by FBP. Each column show the same size of cluster with different MGDs. All images in a column have the same window, level, and contrast.
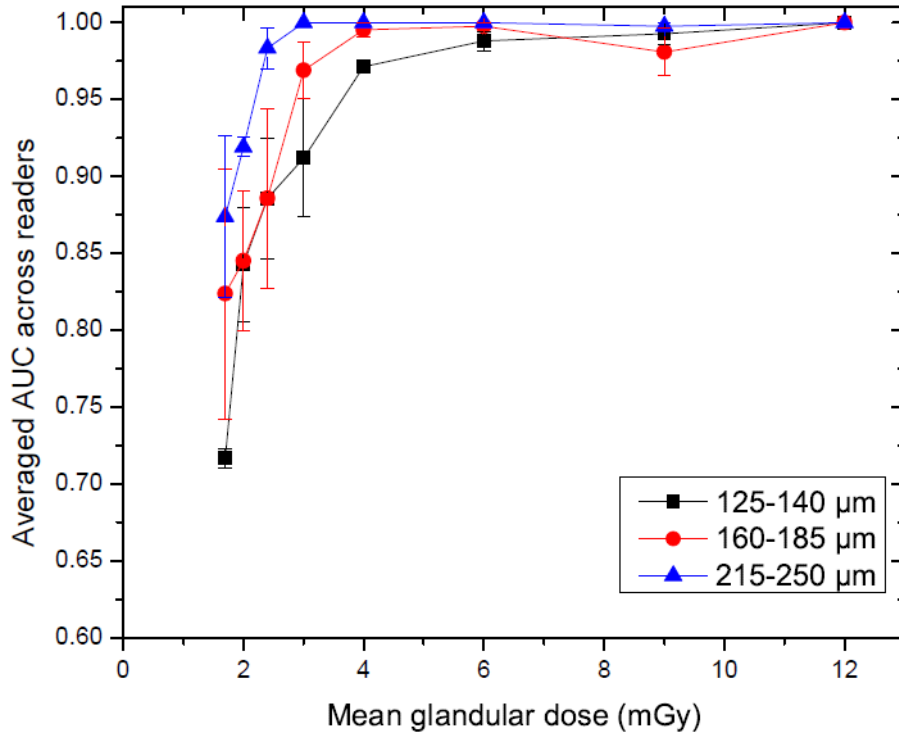
Fig. 9. The average AUC for various microcalcification sizes as a function of MGD with error bars indicating the standard deviation among observers for postmortem for FBP reconstruction algorithms.

Table II. Confidence intervals of 95% for treatment AUC differences. CI: Confidence Interval.

MGD	Treatment comparison	Treatment AUC difference	Std. error difference	z-value	p-value	95% CI
1.7 mGy	140-250	-0.157	-0.04623	3.40	0.0007	[0.0417 , -0.3561]
2 mGy	140-250	-0.076	0.03078	-2.47	0.0134	[-0.2086 , 0.0563]
2.4 mGy	140-250	-0.098	0.02608	-3.74	0.0002	[-0.2098 , 0.0146]
	185-250	-0.098	0.04490	-2.17	0.0298	[-0.2908 , 0.0956]
3 mGy	140-185	-0.057	0.01972	-2.90	0.0038	[-0.1420 , 0.0277]
	140-250	-0.088	0.03832	-2.30	0.0215	[-0.2530 , 0.0768]
6 mGy	140-185	-0.010	0.00393	-2.43	0.0152	[-0.0264 , 0.0074]

Averaged AUCs for all sizes of MCs at all doses across readers are presented in figure 9. The

average AUC was greater than 0.886 and 0.971 for the MCs of all sizes for doses greater than 2

and 4 mGy, respectively. However, the average AUC of 140 μm, 185 μm and 250 μm decreased

14

correspondingly to 0.171, 0.824, 0.874 at 1.7 mGy. The ROC curves for each size of MCs at 1.7, 2.4, 4 and 9 mGy from a radiologist with 8 years of experience are shown in figure 10a, 10b and 10c. The mean AUC differences, standard error differences, z-test, p-value hypothesis test, and 95% confidence intervals are listed in table II for significant (p < 0.05) AUC differences between different sizes at the same dose level. The AUC differences between 160-185 μm and 215-250 μm were not significant at all dose levels except 2.4 mGy, while that between 140 μm and 250 μm were significant at all dose level except 6 mGy.

(a)

(b)

(C)

Fig. 10. The ROC curve of 8-year-experience reader for (a) 140 μm, (b) 185 μm, (c) 250 μm microcalcifications at 1.7 mGy, 2.4 mGy, 4 mGy, and 9 mGy..

4. DISCUSSION
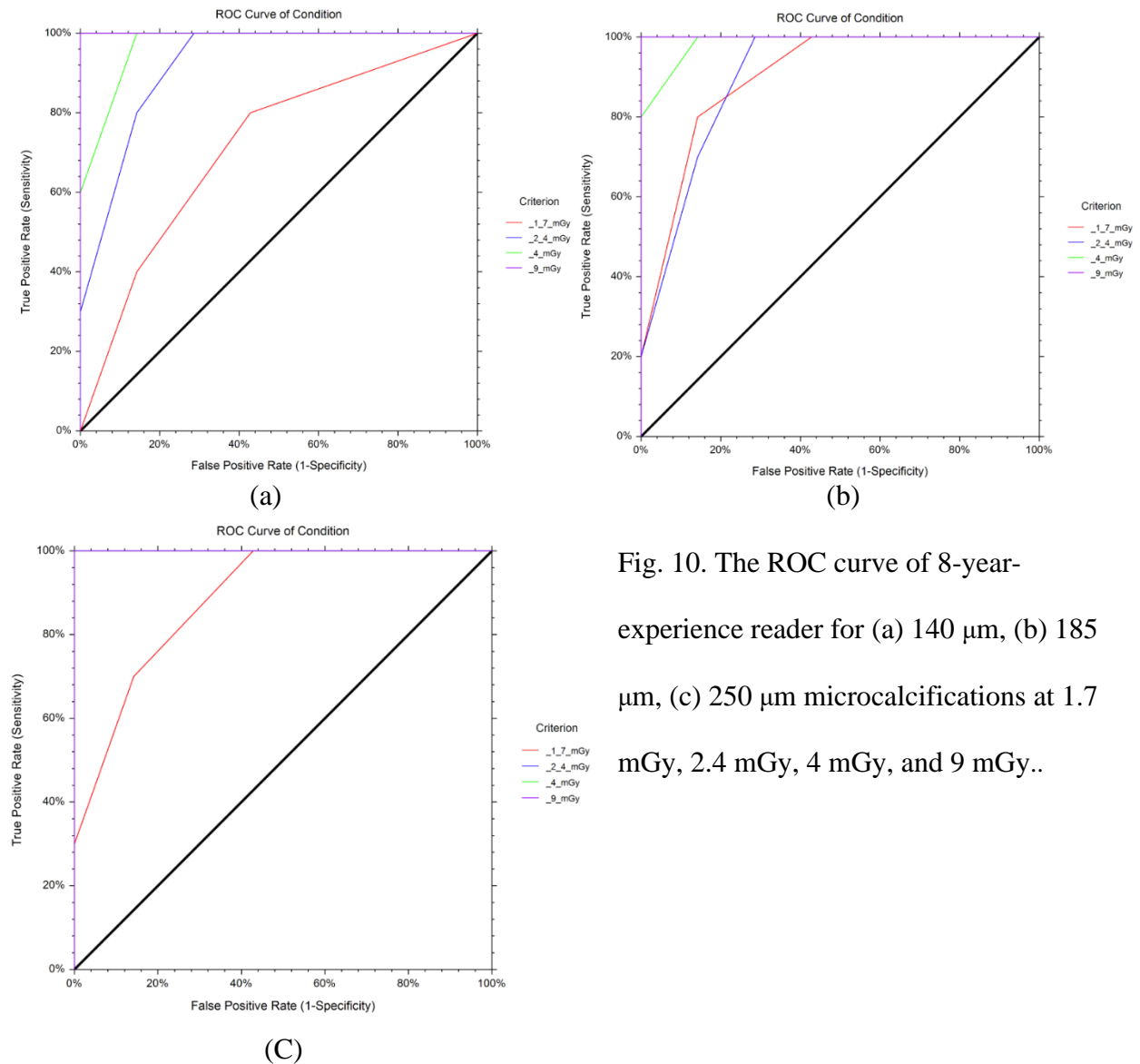
In this study, our CT system prototype coupled with the photon-counting detector of 75 μm^2 pixel size was proposed to evaluate the microcalcification and target sizes in the postmortem breast and ACR phantom. We used 65kVp for the x-ray tube with a 20 keV threshold to capture the strong electric signal of calcification, reduce the electronic and quantum noise and eventually improve the SNR in the projection and reconstructed images. The choice of voltage was supported by the optimized breast CT x-ray spectrum from 50 kV to 60 kV.[17]

The reader study of the ACR phantom using AIR method showed an average score of 5.5, 3.5, 4.5 for fibers, specks and masses at 3mGy, respectively, which were higher than the corresponding scores from FBP images. The scores of AIR images at 3 mGy satisfied the minimum performance criteria of the 4 fibers, 3 speck groups, and 3 masses regulated by the American College of Radiology.[15] It also satisfied the minimum requirements of 5 fibers and 4 masses of a commercial digital mammography machine, except a missing score of 0.5 from its requirement of 4 specks.[18]

A study reported the MGD of 1.8 mGy and 2.1 mGy to obtain the best image quality in ACR phantom using FFDM machine and film-screen mammography machine (FSM), respectively.[19] Although our result that met the minimum requirement for ACR and commercial digital mammography machine was higher than the MGD reported in the study, the value was comparable to clinical CC-view MGD of 3.37 mGy in FFDM.[20]

The reader study of postmortem breast showed advancement in detecting smaller MCs at a lower dose compared to multiple research findings. A previous reported cone-beam CT system with flat panel detector showed a minimum detectable MCs size of 348±2 μm at a MGD of 3 mGy.[20] Another study using spiral CT approach with a CdTe photon-counting detector showed improvement with clear detectability of 150 μm MCs at a MGD of 3mGy.[21] In addition, a study reported bench-top photon-counting breast CT system with a Si strip detector showed an experimental result of AUC greater than 0.89±0.07 for MCs greater than 120 μm at MGD of 3 mGy, and an AUC less than 0.83 for MCs smaller than 140 μm below 3 mGy.[22]

Our experimental results with the postmortem breast indicated an improvement in detectability of MCs using the proposed CdTe photon-counting breast CT system. The MCs larger than 125 μm were detectable with AUC greater than 0.912±0.038 at a MGD of 3 mGy, and maintained an AUC greater than 0.843±0.038 at a mean glandular dose of 2 mGy.

While our results showed improvement of detectability of MCs at a lower dose using the CdTe photon-counting detector, there were limitations in MCs preparation, corrections and reconstructions. First, the calcium carbonate specks used in postmortem breast scanning were not uniformly distributed across the insert. A notable drop in AUC at 125 – 140 μm MCs from 2 mGy to 1.7 mGy, while the AUCs of 160- 185 μm and 215-250 μm MCs decrease gradually across the range of MGD. The actual size range of 125-140 μm calcium specks sampled for reader study might be revealed to be at the lower end of the range.

Second, a noticeable ring artifact was shown in reconstructed images using both FBP and AIR methods. The ring might come from the analytically corrected intermodular gaps, which could

not perfectly recover the information lost in the pixels. However, the slight ring artifacts did not affect the sampling of MCs and phantom screening in both reader study. Similarly, another study with ring artifact on all images showed no limitation to the examination of lesions and MCs.[23]

Third, the mean sizes of single MC are larger than the reference size stated in table II, which could potentially be due to the edges blurring by noise and partial volume effect from the reconstructions. Both analytical and machine learning techniques had proven to reduce the partial volume effect, which improved the image quality and could reveal the high-density MCs.[24,25]

5. CONCLUSION

The results specified the proposed CT system prototype with the CdTe photon-counting detector could detect a smaller size of specks with improved spatial resolution in both ACR phantom and postmortem breast. A higher AUC of microcalcification detection was introduced comparing with other photon-counting breast CT system at a lower radiation dose.

6. FUTURE WORK

The postmortem breast IR images will be reconstructed, and a corresponding reader study will be conducted to investigate the improvement of MC detectability compared with FBP reconstruction. Furthermore, the spectral information of the photon-counting detector will be investigated to perform spectral distortion correction on the projections to reduce the influence of pulse pileup and charge sharing. Optimal weighting techniques will be applied after recovering of distorted spectrum to further improve the CNR by giving higher weight to the lower energy

photons. Iterative reconstruction utilizing the spectral information of the detector will be performed to further improve the CNR and spatial resolution.

7. REFERENCE

[1]Siegel RL, Miller KD, Jemal A. Cancer statistics, 2022. CA Cancer J Clin. 2022;72:7-33.

[2]Pfeiffer RM, Webb-Vargas Y, Wheeler W, Gail MH. Proportion of U.S. Trends in Breast Cancer Incidence Attributable to Long-term Changes in Risk Factor Distributions. *Cancer Epidemiol Biomarkers Prev*. 2018;27(10):1214-1222.

[3]Henrot P, Leroux A, Barlier C, Génin P. Breast microcalcifications: the lesions in anatomical pathology. *Diagn Interv Imaging*. 2014;95(2):141-152.

[4]Lai CJ, Shaw CC, Chen L, et al. Visibility of microcalcification in cone beam breast CT: effects of X-ray tube voltage and radiation dose. *Med Phys*. 2007;34(7):2995-3004.

[5]Kleinknecht JH, Ciurea AI, Ciortea CA. Pros and cons for breast cancer screening with tomosynthesis - a review of the literature. *Med Pharm Rep*. 2020;93(4):335-341.

[6]O'Connell A, Conover DL, Zhang Y, et al. Cone-beam CT for breast imaging: Radiation dose, breast coverage, and image quality. *AJR Am J Roentgenol*. 2010;195(2):496-509.

[7]Rößler AC, Kalender W, Kolditz D, et al. Performance of Photon-Counting Breast Computed Tomography, Digital Mammography, and Digital Breast Tomosynthesis in Evaluating Breast Specimens. *Acad Radiol*. 2017;24(2):184-190.

[8]Wienbeck S, Lotz J, Fischer U. Review of clinical studies and first clinical experiences with a commercially available cone-beam breast CT in Europe. *Clin Imaging*. 2017;42:50-59.

[9]A. C. Kak and Malcolm Slaney, *Principles of Computerized Tomographic Imaging,* IEEE Press, 1988.

[10]Gao H. Fused analytical and iterative reconstruction (AIR) via modified proximal forward-backward splitting: a FDK-based iterative image reconstruction example for CBCT. *Phys Med Biol*. 2016;61(19):7187-7204.

[11]Herman GT. Correction for beam hardening in computed tomography. *Phys Med Biol*. 1979;24(1):81-106.

[12]Parker DL. Optimal short scan convolution reconstruction for fanbeam CT. *Med Phys*. 1982;9(2):254-257.

[13]Parikh N, Boyd S. Proximal algorithms. *Found. Trends Optim*. 2013;1:123–231

[14]Sidky, Emil Y, and Xiaochuan Pan. "Image reconstruction in circular cone-beam computed tomography by constrained, total-variation minimization." *Physics in medicine and biology* vol. 53,17 (2008): 4777-807.

[15]Hendrick RE, Bassett L, Botsco MA, et al. *Mammography Quality Control Manual.* Reston, Va: American College of Radiology; 1999.

[16]DeLong ER, DeLong DM, Clarke-Pearson DL. Comparing the areas under two or more correlated receiver operating characteristic curves: a nonparametric approach. *Biometrics*. 1988;44(3):837-845.

[17]Kuttig JD, Steiding C, Kolditz D, Hupfer M, Karolczak M, Kalender WA. Comparative investigation of the detective quantum efficiency of direct and indirect conversion detector technologies in dedicated breast CT. *Phys Med*. 2015;31(4):406-413.

[18]Selenia Dimensions digital mammography system and digital tomosynthesis system quality control manual. MAN-01965 revision 010. Hologic, Bedford, Mass.

[19]Rezapour J, Mostear A, Tarighatnia A et al. Trade-off between breast mean glandular dose and image quality in digital and conventional mammogram systems: A multicenter study. *Radioprotection*. (2021);56(3), 221-227.

[20]Teoh KC, Manan HA, Mohd Norsuddin N, Rizuana IH. Comparison of Mean Glandular Dose between Full-Field Digital Mammography and Digital Breast Tomosynthesis. *Healthcare (Basel)*. 2021;9(12):1758.

[21]Kalender WA, Beister M, Boone JM, Kolditz D, Vollmar SV, Weigel MC. High-resolution spiral CT of the breast at very low dose: concept and feasibility considerations. *Eur Radiol*. 2012;22(1):1-8.

[22]Cho HM, Ding H, Barber WC, Iwanczyk JS, Molloi S. Microcalcification detectability using a bench-top prototype photon-counting breast CT based on a Si strip detector. *Med Phys*. 2015;42(7):4401-4410.

[23]Berger N, Marcon M, Saltybaeva N, et al. Dedicated Breast Computed Tomography With a Photon-Counting Detector: Initial Results of Clinical In Vivo Imaging. *Invest Radiol*. 2019;54(7):409-418.

[24]Šprem J, de Vos BD, Lessmann N, et al. Coronary calcium scoring with partial volume correction in anthropomorphic thorax phantom and screening chest CT images. *PLoS One*. 2018;13(12):e0209318.

[25]Daimiel Naranjo I, Gibbs P, Reiner JS, et al. Breast Lesion Classification with Multiparametric Breast MRI Using Radiomics and Machine Learning: A Comparison with Radiologists' Performance. *Cancers (Basel)*. 2022;14(7):1743.